EDGE ARTICLE

CrossMark
click for updates

Regulating the active species of Ni(OH)$_2$ using CeO$_2$: 3D CeO$_2$/Ni(OH)$_2$/carbon foam as an efficient electrode for the oxygen evolution reaction†

Zhengqing Liu,[a] Na Li,[a] Hongyang Zhao,[a] Yi Zhang,[b] Yunhui Huang,[bc] Zongyou Yin[de] and Yaping Du*[a]

Three dimensional (3D) N, O and S doped carbon foam (NOSCF) is prepared as a substrate for *in situ* vertically grown Ni(OH)$_2$ nanosheets. As designed Ni(OH)$_2$/NOSCF possesses strong electrostatic interactions with OH$^-$ ions due to many C=O groups existing in NOSCF, which can facilitate the formation of crucial NiOOH intermediates during the OER process. CeO$_2$ nanoparticles (NPs) of ~3.3 nm in size are decorated on Ni(OH)$_2$ nanosheets to design a highly efficient CeO$_2$/Ni(OH)$_2$/NOSCF electrocatalyst for the oxygen evolution reaction (OER). The CeO$_2$ NP decorated Ni(OH)$_2$/NOSCF not only exhibits a remarkably improved OER performance with an onset potential of 240 mV, outperforming most reported non-noble metal based OER electrocatalysts, but also possesses a small Tafel slope of 57 mV dec^{-1} and excellent stability under different overpotentials. The synergistic effect of producing more active species of Ni$^{III/IV}$ and accelerating the charge transfer for Ni(OH)$_2$/NOSCF by the introduction of CeO$_2$ NPs is also investigated. These results demonstrate the possibility of designing energy efficient OER catalysts with the assistance of earth abundant CeO$_2$-based catalysts.

Introduction

Clearly, using electricity to split water into hydrogen and oxygen (2H$_2$O → 2H$_2$ + O$_2$) is one of the most efficient and attractive methods for the production of renewable energy.[1,2] However, large-scale water electrolysis is greatly hindered due to the huge overpotential and significant efficiency loss for the half-cell of the oxygen evolution reaction (OER).[3–5] Although noble-metal based materials (*e.g.* Ir, Pt) are currently regarded as high-efficiency OER catalysts, their low earth abundance and high cost limit their widespread use.[6–8] Therefore, in recent years,

various efficient and low-cost OER electrocatalysts (such as, Fe, Co, Ni and Mn) with high OER performance (low onset potential, high activity and good stability) in basic electrolytes have been extensively designed and investigated.[8–23] Among them, nickel(II) hydroxide (Ni(OH)$_2$)-based materials are attractive electrocatalysts for the OER because of their intrinsic potential for high OER performance and two-dimensional (2D) layered structure.[20] Another key reason for the extensive study of Ni(OH)$_2$ is that the high oxidation state of Ni$^{III/IV}$ can serve as an active species for OER catalysts.[24] For example, Ye *et al.* prepared a Ni(OH)$_2$–Au hybrid as an OER catalyst, and a significantly enhanced OER performance was exhibited by enhancing the generation of the Ni$^{III/IV}$ active species. However, the poor kinetics and mass-transferability of Ni(OH)$_2$ as an electrocatalyst for the OER still limit its further development for practical applications.

Cerium(IV) oxide (CeO$_2$) is one of the most important rare earth oxides, is stable in alkaline solution, converts easily between the Ce^{3+} and Ce^{4+} oxidation states, undergoes reversible oxygen ion exchange (1/2O$_2$ (gas) + 2e$^-$ (solid) ↔ O^{2-} (solid)), and has good ionic conductivity and high oxygen-storage capacity (OSC).[25–27] The above unique properties enable CeO$_2$ to serve as a cocatalyst to enhance the performance of OER catalysts by improving charge transfer and energy conversion efficiency, which can also solve the poor kinetics and mass-transferability problems of Ni(OH)$_2$ for the OER. However,

[a]Frontier Institute of Science and Technology Jointly with College of Science, State Key Laboratory for Mechanical Behavior of Materials, Xi'an Jiaotong University, 99 Yanxiang Road, Yanta District, Xi'an, Shaanxi Province 710054, China. E-mail: ypdu2013@mail.xjtu.edu.cn

[b]Collaborative Innovation Center of Intelligent New Energy Vehicle, School of Materials Science and Engineering, Tongji University, Shanghai 201804, P. R. China

[c]State Key Laboratory of Material Processing and Die & Mould Technology, School of Materials Science and Engineering, Huazhong University of Science and Technology, Wuhan, Hubei 430074, P. R. China

[d]Research School of Chemistry, The Australian National University, Canberra, Australian Capital Territory 2601, Australia

[e]Department of Materials Science and Engineering, Massachusetts Institute of Technology, Cambridge, MA 02139, USA

† Electronic supplementary information (ESI) available: Full experimental procedures, experimental section, XPS spectra, TEM images, FTIR spectra and other electrochemical performance data. See DOI: 10.1039/c6sc05408k

few studies have focused on the application of CeO_2 nano-crystals in the electrocatalytic field. Recently, Li et al. developed an efficient OER electrocatalyst by supporting $FeOOH/CeO_2$ on Ni foam and exhibited enhanced OER performance compared with pure FeOOH.[28] They also demonstrated the unique high OSC properties of CeO_2, such that CeO_2 can straightway absorb the oxygen produced during the OER and accordingly promote the OER. Therefore, the combination of $Ni(OH)_2$ and CeO_2 to form a $CeO_2/Ni(OH)_2$ hybrid will be an efficient route to improve the electrocatalytic performance of $Ni(OH)_2$ via improving the energy conversion efficiency, and thereby promoting the generation of active species of $Ni^{III/IV}$ for enhancing the OER performance.
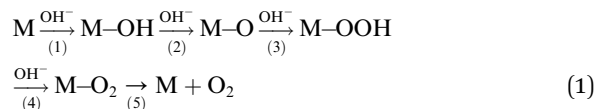
In order to greatly prevent the $Ni(OH)_2$ nanosheets from aggregation and thus further enhance the OER performance, three dimensional (3D) free-standing carbon foam (CF) is chosen as the substrate for in situ growth of the $Ni(OH)_2$ nanosheets. The advantages of applying such 3D CF as a substrate can be attributed to the interconnected frameworks with large surface area for effective contact with an aqueous electrolyte and rapid interfacial electron charge transfer. Moreover, the obtained CF is doped by N, O and S elements during carbonization without other extra chemicals being added, where the N, O and S elements come from the melamine resin and sodium bisulfite additive of melamine foam (MF) (Fig. S1, ESI†). And N, O and S doped carbon materials are believed to enhance the OER activity.[29]

Herein, as we expect, $Ni(OH)_2$ nanosheets are successfully grown along the frameworks of N, O and S doped CF (NOSCF) and prevent the undesirable aggregation of $Ni(OH)_2$ nanosheets because of the open cell pores of NOSCF. Then, we prepared uniform CeO_2 NPs of ∼3.3 nm in size via a one step colloidal synthesis method, and deposited the surface modified-CeO_2 NPs on $Ni(OH)_2$ nanosheets of the as-designed $Ni(OH)_2/NOSCF$ to form a self-supported $CeO_2/Ni(OH)_2/NOSCF$ electrode, as shown in Fig. 1. As a result of the open cell structure of 3D NOSCF for facile electrolyte transport and strong electronic interactions between CeO_2 NPs and $Ni(OH)_2$ nanosheets for accelerating the oxidation of Ni^{II} to $Ni^{III/IV}$, the $CeO_2/Ni(OH)_2/NOSCF$ electrocatalyst delivers an excellent water oxidation performance at a lower onset potential, ranking high among the extensive non-noble electrocatalysts studied for the OER. As we know, this is the first time CeO_2 is combined with a functional $Ni(OH)_2$ electrocatalyst, which offers an impressive OER performance, and provides insight into the possibility of enhancing OER catalysis by using rare earth CeO_2-based nanomaterials.

Results and discussion

Design of the $CeO_2/Ni(OH)_2/NOSCF$ electrocatalyst

N, O and S doped CF was prepared by direct carbonization of melamine foam (MF) in a tube furnace at 700 °C for 1 h under protection of a nitrogen atmosphere. After carbonization, the volume of CF shrunk to about 70% of MF (inset of Fig. 2a). Then, the NOSCF was further oxidized by dipping into a mixture of acids of HNO_3 (65%) and H_2SO_4 (98%) with a volume ratio of 1 : 3 for 6 h, which can produce more C=O groups (Fig. S2a, ESI†).[29] It has been revealed that the C atoms in the C=O groups have a stronger electrostatic interaction with OH^- ions than other oxygen-containing groups, which can facilitate the formation of crucial M–OOH intermediates (eqn (1)), and thus accelerate the OER reaction.[30,31]

$$M \xrightarrow[(1)]{OH^-} M–OH \xrightarrow[(2)]{OH^-} M–O \xrightarrow[(3)]{OH^-} M–OOH$$
$$\xrightarrow[(4)]{OH^-} M–O_2 \xrightarrow[(5)]{} M + O_2 \tag{1}$$

The elemental content in the NOSCF was measured by XPS analysis to be about 66.8, 4.3, 24.5 and 0.42 atom% for C, N, O and S, respectively (Fig. S2b, ESI†). Scanning electron microscopy (SEM) images in the inset of Fig. 2a revealed that the as-prepared NOSCF possessed an interconnected network architecture, which could make it an ideal substrate for the growth of some electrocatalysts. Then, by using the framework of NOSCF as a nucleation platform, $Ni(OH)_2$ nanosheets could be uniformly grown in situ along the framework of NOSCF by a simple chemical bath deposition process,[32] which could be observed evidently from the SEM images (Fig. 2b and c). The selective growth of $Ni(OH)_2$ nanosheets on the NOSCF could preserve the open-cell structure of the NOSCF (Fig. 2b) and efficiently prevent the aggregation of $Ni(OH)_2$ nanosheets, indicating that it held a large surface area for electrocatalysis. The vertical $Ni(OH)_2$ layers could be clearly observed in an enlarged SEM image of the $Ni(OH)_2$/carbon foam hybrid (Fig. S3, ESI†). Such nanostructured materials can offer a much rougher surface, which reduces the solid–gas interaction, giving rise to a timely release of adhered gas bubbles and thus enhancing the OER performance.

The grown $Ni(OH)_2$ nanosheets had a hexagonal phase ($a = b = 0.308$ nm, $c = 0.234$, JCPDS: 38-0715), as confirmed by powder X-ray diffraction (PXRD) analysis (Fig. 2d). As shown in the transmission electron microscopy (TEM) image in Fig. 2e, the grown $Ni(OH)_2$ presented a typical layered structure, and the

Fig. 1 Process for the design of a self-supported $CeO_2/Ni(OH)_2/NOSCF$ electrode and application for the oxygen evolution reaction.
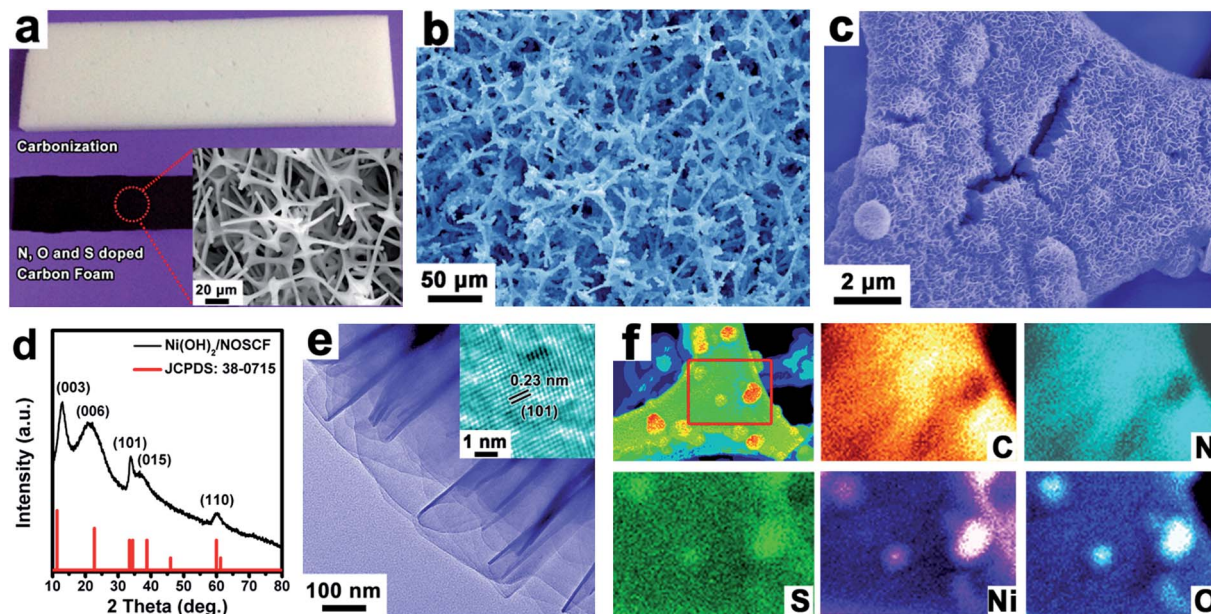
Fig. 2 (a) A piece of melamine foam derived carbon foam. (b and c) SEM images of Ni(OH)$_2$ nanosheets grown on NOSCF and the corresponding (d) XRD pattern. (e) HRTEM image of synthesized Ni(OH)$_2$ recorded from the edge of the Ni(OH)$_2$/NOSCF. (f) EDS elemental mapping for C, N, S, Ni and O elements recorded on the Ni(OH)$_2$/NOSCF.

high resolution (HRTEM) image (inset of Fig. 2e) identified the (101) plane of a hexagonal crystal structure for the Ni(OH)$_2$ nanosheets with an interplanar spacing of 0.23 nm. The corresponding elemental mapping of the designed Ni(OH)$_2$/NOSCF is shown in Fig. 2f; the C, N and S elements were distributed on the whole surface of the frameworks in the NOSCF, and also displayed a very uniform distribution of Ni(OH)$_2$. The loading percentage of Ni(OH)$_2$ in the Ni(OH)$_2$/NOSCF composite was estimated to be ~63% by thermogravimetric analysis (TGA), as displayed in Fig. S4 (ESI†).

The CeO$_2$ NPs were synthesized by using cerium(IV) ammonium nitrate ((NH$_4$)$_2$Ce(NO$_3$)$_6$) as a precursor in a mixture of solvents of oleylamine and 1-octadecene. As shown in the PXRD pattern in Fig. 3a, the prepared CeO$_2$ samples presented a cubic phase (space group: $Fm\bar{3}m$, $a = b = c = 5.411$ Å, JCPDS: 34-0394). The TEM image in Fig. 3b showed that the as-synthesized CeO$_2$ NPs were relatively monodisperse with an average size of ~3.3 nm (inset of a histogram of the particle diameters). The good monodispersity of the CeO$_2$ NPs indicates the retention of the used capping ligand (oleylamine) on the surface of CeO$_2$ NPs, as demonstrated by Fourier transform infrared (FTIR) spectroscopy (Fig. S5, ESI†). As seen in Fig. 3c, the HRTEM image of the CeO$_2$ NPs showed clearly crystal lattice fringes with an interplanar spacing of 0.16 nm, which can be ascribed to the (111) crystal plane. The selected area electron diffraction (SAED) pattern shown in Fig. 3d indicated that the synthesized CeO$_2$ NPs were highly crystallized.

The prepared CeO$_2$ NPs are hydrophobic due to the long carbon chains of oleylamine (OM) used as surfactants for the reaction, and hence cannot directly disperse in water. In order to generate a hydrophilic surface for combining with the Ni(OH)$_2$/NOSCF and testing the OER performance, we employed

NaS$_2$ solution to modify the surface of CeO$_2$ NPs (Fig. S5, ESI†).[33] As shown in the TEM image in Fig. S6a (ESI†), the CeO$_2$ NPs still kept their particle morphology with high crystallization after surface modification, and could be well dispersed in water (digital photo in Fig. S6b, ESI†). The CeO$_2$ NPs were anchored on the Ni(OH)$_2$/NOSCF using a controllable electrophoretic deposition strategy, the details are shown in the Experimental section.[34] All of the diffraction peaks of Ni(OH)$_2$ (JCPDS: 380715) and CeO$_2$ (JCPDS: 34-0394) were detected in CeO$_2$/Ni(OH)$_2$/NOSCF (Fig. 4a). Fig. 4b and c show the representative TEM and HRTEM images of the CeO$_2$/Ni(OH)$_2$ hybrid obtained from CeO$_2$/Ni(OH)$_2$/NOSCF with a deposition duration of 10 min. It can be observed from Fig. 4b that the Ni(OH)$_2$ nanosheets are uniformly decorated with CeO$_2$ NPs. Fig. 4c presents the corresponding HRTEM image with an interplanar spacing of 0.16 nm and 0.23 nm, indexed to the (111) and (101) crystal planes of CeO$_2$ and Ni(OH)$_2$, respectively.

To further investigate the strong electronic interactions between Ni(OH)$_2$ nanosheets and CeO$_2$ NPs, UV-vis absorption spectra (Fig. 4d) and X-ray photoelectron spectroscopy (XPS) spectra (Fig. 4e and f) of Ni(OH)$_2$ nanosheets, CeO$_2$ NPs and the CeO$_2$/Ni(OH)$_2$ hybrid were examined. As shown in Fig. 4d, two absorption peaks of the grown Ni(OH)$_2$ nanosheets located at 385 and 670 nm corresponded to the d–d transitions of Ni^{II} cations.[35] Compared with the pristine Ni(OH)$_2$ nanosheets, the absorption spectrum of CeO$_2$/Ni(OH)$_2$ was obviously red-shifted (~8 nm), indicating the strong electronic interactions between them.[36,37] XPS spectra of Ce 3d and Ni 2p are shown in Fig. 4e and f, respectively. As shown in Fig. 4e, for Ce 3d of CeO$_2$, the peaks located at 920–911 eV and 903–893 eV correspond to Ce 3d$_{3/2}$, and the peaks located at 877–866 eV correspond to Ce 3d$_{5/2}$, which demonstrated the coexistence of Ce^{3+} and Ce^{4+} in the
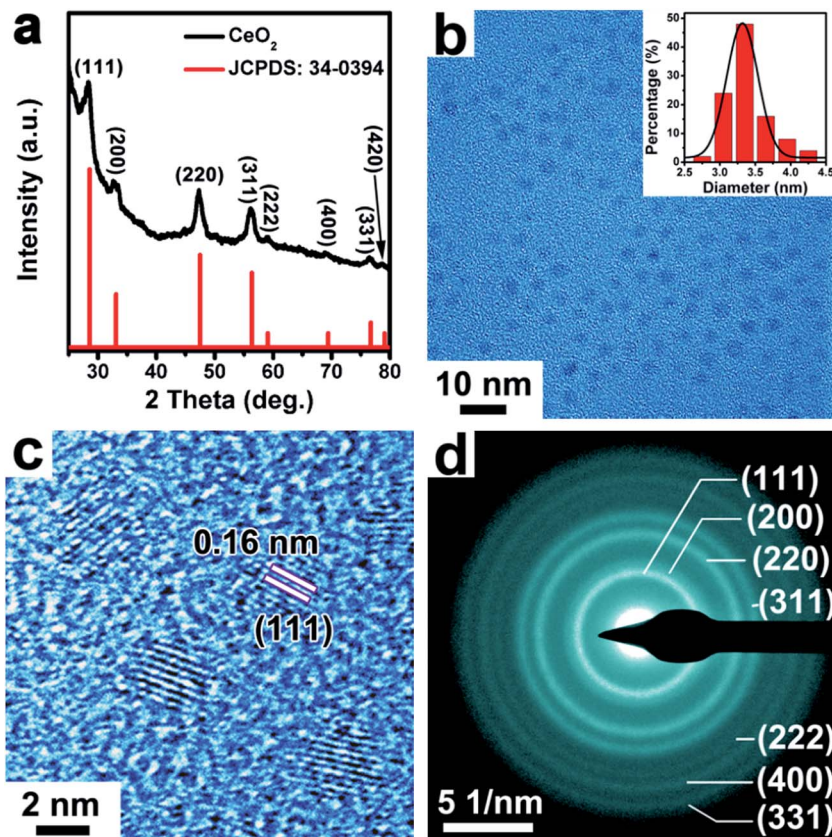
Fig. 3 (a) XRD pattern of the obtained CeO_2 sample. (b) TEM, (c) HRTEM image and (d) corresponding SAED pattern of synthesized ~3.3 nm sized CeO_2 NPs. Inset of (b): a particle size distribution analysis.

CeO_2 NPs.[38] However, after CeO_2 NPs were deposited on the $Ni(OH)_2$ nanosheets, the ratio of $Ce^{3+} : Ce^{4+}$ in the $CeO_2/Ni(OH)_2$ hybrid changed compared with pure CeO_2 NPs, indicating that the valence states of Ce in the $CeO_2/Ni(OH)_2$ hybrid rearranged.[28] As shown in Fig. 4f, the XPS spectrum of Ni 2p in $Ni(OH)_2$/NOSCF showed two major peaks at 853.2 and 870.8 eV corresponding to Ni $2p_{3/2}$ and Ni $2p_{1/2}$, respectively, which were characteristic of the Ni^{2+} state.[39] And some satellite peaks in the Ni 2p region could also be observed in Fig. 4f. Through careful comparison and analysis, we found that the peaks of Ni $2p_{3/2}$ and Ni $2p_{1/2}$ in the XPS spectrum for $CeO_2/Ni(OH)_2$/NOSCF both shifted to lower binding energies of ~0.5 eV. Therefore, the ratio change of Ce 3d and peak shifts of Ni 2p in the $CeO_2/Ni(OH)_2$ hybrid indicate strong electronic interactions between the $Ni(OH)_2$ nanosheets and CeO_2 NPs.

$CeO_2/Ni(OH)_2$/NOSCF electrocatalyst for OER performance

The water oxidation reaction was applied to study the electronic interactions between $Ni(OH)_2$ nanosheets and CeO_2 NPs and their effect on the corresponding catalytic activity. The OER performance of the $CeO_2/Ni(OH)_2$/NOSCF electrocatalyst was investigated in 1.0 M KOH (pH = 14). As a comparison, $Ni(OH)_2$/NOSCF, CeO_2/NOSCF, NOSCF and Ir/C were also tested under the same conditions. It was obvious from the cyclic voltammetry (CV) curves (Fig. 5a) that both the electrocatalysts of $Ni(OH)_2$/

NOSCF and $CeO_2/Ni(OH)_2$/NOSCF clearly showed redox peaks ranging from 1.2 to 1.6 V, which belong to the $Ni^{II}/Ni^{III/IV}$ redox process ($Ni(OH)_2 + OH^- \rightarrow NiOOH + H_2O + e^-$). And there was an obvious negative shift of the oxidation potential, changed from 1.46 V to 1.41 V for $CeO_2/Ni(OH)_2$/NOSCF, indicating that $CeO_2/Ni(OH)_2$/NOSCF has higher transfer efficiency from Ni^{II} to $Ni^{III/IV}$ and larger charge capacity than $Ni(OH)_2$/NOSCF.[40] This conclusion can be further demonstrated by Nyquist plots. As presented in Fig. S7 (ESI†), compared with $Ni(OH)_2$/NOSCF, the $CeO_2/Ni(OH)_2$/NOSCF shows a smaller charge transfer resistance (high frequencies) and reduced mass-transfer resistance (low frequencies). The decrease in mass transfer resistance may contribute to the increased number of $Ni^{III/IV}$ active species.

As shown in the polarization curves in Fig. 5b and statistical data in Fig. 5c, the $CeO_2/Ni(OH)_2$/NOSCF exhibited a lower onset potential of 240 mV than Ir/C and $Ni(OH)_2$/NOSCF, surpassing most reported non-noble metal based OER electrocatalysts (Table S1, ESI†). In particular, the significant increase of the current density was more obvious when the potential was beyond ~1.6 V, which could further demonstrate that the OER activity of $Ni(OH)_2$/NOSCF is greatly enhanced when decorated with CeO_2 NPs. In addition, we also optimized the loaded mass ratio of CeO_2 NPs on $Ni(OH)_2$/NOSCF and found that when the mass ratio of CeO_2: $Ni(OH)_2$/NOSCF was 30% (Fig. S8, ESI†), the electrocatalytic activity of $CeO_2/Ni(OH)_2$/NOSCF reached its highest level, and therefore this mass ratio was used in the following experiments.
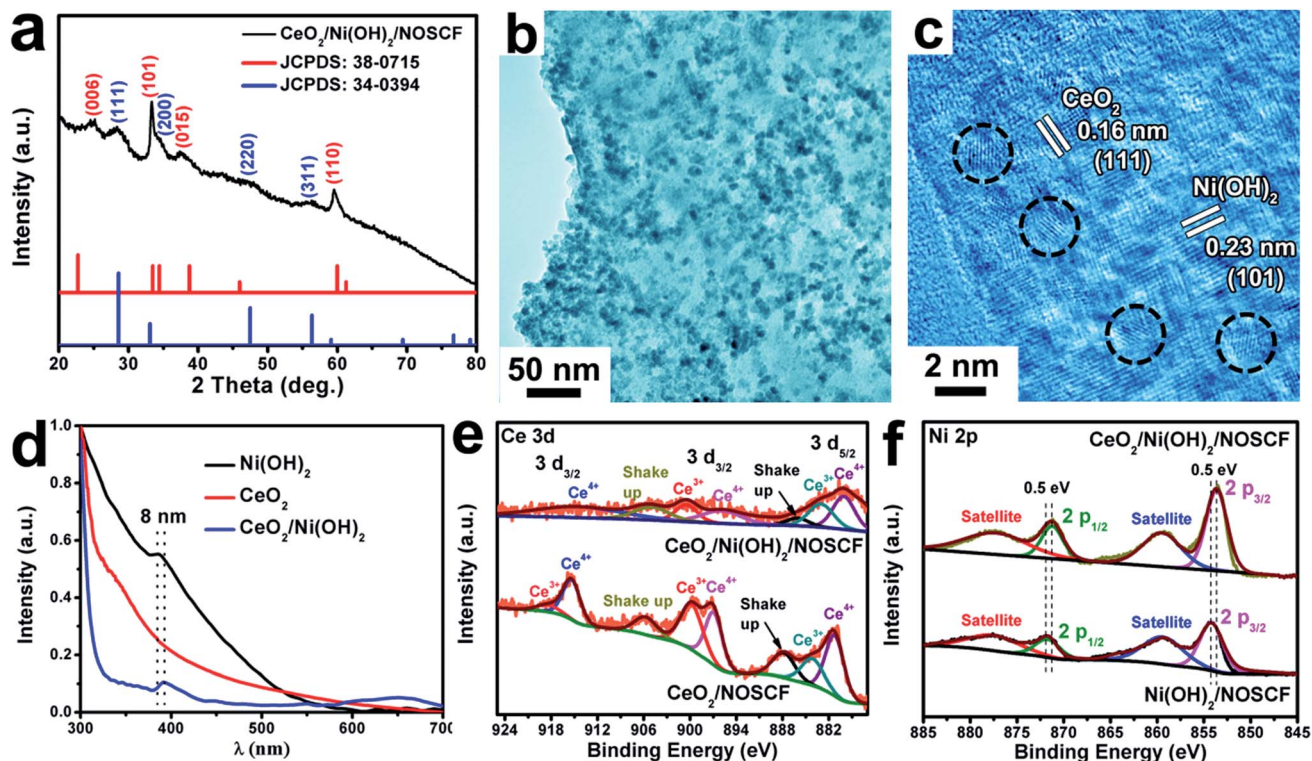
Fig. 4 (a) XRD pattern, (b) TEM and (c) HRTEM images of $CeO_2/Ni(OH)_2$ hybrid nanostructures obtained from the $CeO_2/Ni(OH)_2/NOSCF$. (d) UV-vis absorption spectra of pristine $Ni(OH)_2$ nanosheets, CeO_2 NPs and the $CeO_2/Ni(OH)_2$ hybrid. A comparison of (e) Ce 3d and (f) Ni 2p high-resolution XPS spectra of $CeO_2/Ni(OH)_2/NOSCF$ and $Ni(OH)_2/NOSCF$.
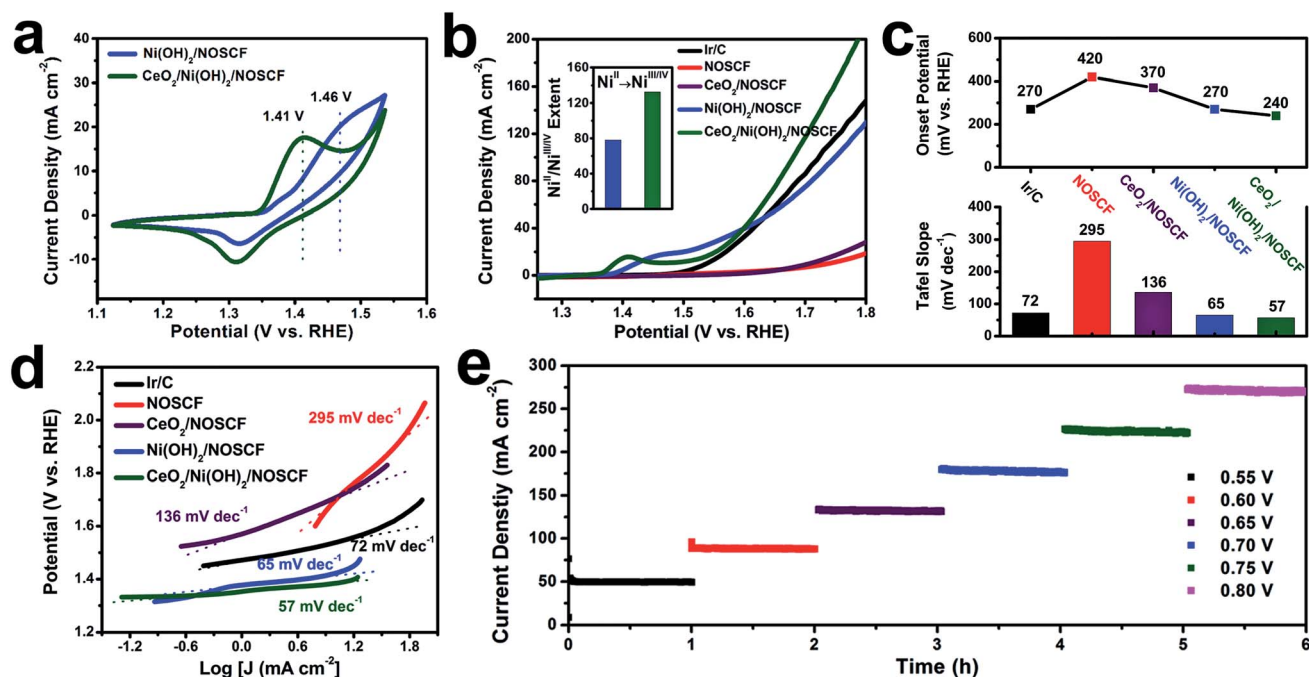

Fig. 5 (a) CV curves of $Ni(OH)_2/NOSCF$ and $CeO_2/Ni(OH)_2/NOSCF$. (b) Polarization curves of NOSCF, $CeO_2/NOSCF$, $Ni(OH)_2/NOSCF$, $CeO_2/Ni(OH)_2/NOSCF$ and the benchmark Ir/C electrocatalyst for comparison. Sweep rate: 5 mV s^{-1}. Inset: the extent of Ni^{II}/Ni$^{III/IV}$ transformation for $Ni(OH)_2/NOSCF$ and $CeO_2/Ni(OH)_2/NOSCF$. (c and d) The corresponding onset potential and Tafel curves for the catalysts derived from (b). (e) Stability test using a continuous OER recorded on the $CeO_2/Ni(OH)_2/NOSCF$ self-supported electrode under different static potentials (V vs. SCE).

During the OER process, the highly oxidative $Ni^{III/IV}$ cations are believed to serve as active species, which indicates that the enhanced catalytic activity for $CeO_2/Ni(OH)_2/NOSCF$ observed in our study might be a result of increasing $Ni^{II}/Ni^{III/IV}$ transformations. Therefore, we investigated the extent of the $Ni^{II}/Ni^{III/IV}$ transformation by integrated oxidation peak areas (inset of Fig. 5b).[41,42] When CeO_2 NPs were deposited on the $Ni(OH)_2/NOSCF$, the $Ni^{II}/Ni^{III/IV}$ extent showed a dramatic increase of about 1.7-fold compared with the $Ni(OH)_2/NOSCF$ (inset of Fig. 5b), thus CeO_2 NPs potentially facilitated producing more $Ni^{III/IV}$ active species and subsequently led to the improvement of the OER catalytic activity (Fig. 5b).

The enhanced OER activity of $CeO_2/Ni(OH)_2/NOSCF$ was more obvious by comparing the Tafel slopes. As shown in Fig. 5c and d, the Tafel slope of $CeO_2/Ni(OH)_2/NOSCF$ was 57 mV dec^{-1}, and it was smaller than those of Ir/C (72 mV dec^{-1}), NOSCF (295 mV dec^{-1}), $CeO_2/NOSCF$ (136 mV dec^{-1}), and $Ni(OH)_2/NOSCF$ (65 mV dec^{-1}). Through the comparison of the Tafel slopes we could demonstrate that depositing CeO_2 NPs on $Ni(OH)_2/NOSCF$ could facilitate its OER kinetics, and the OER activity of $CeO_2/Ni(OH)_2/NOSCF$ was comparable to many other non-noble metal OER electrocatalysts in alkaline media (Table S1, ESI†).

We also tested the stability of the designed $CeO_2/Ni(OH)_2/NOSCF$ by a chronoamperometry method to evaluate the OER performance. As shown in Fig. 5e, the current density of the OER showed no change during 6 h of continuous operation under various potentials of 0.55, 0.60, 0.65, 0.70, 0.75 and 0.80 V, which suggested that the $CeO_2/Ni(OH)_2/NOSCF$ had excellent stability for the OER process. Thus, the $CeO_2/Ni(OH)_2/NOSCF$ with its high catalytic activity as well as excellent stability would be a promising candidate for electrochemical water oxidation.

Conclusions

In summary, we have successfully designed a 3D hierarchical $Ni(OH)_2/NOSCF$ electrode by growing $Ni(OH)_2$ nanosheets along the carbon frameworks of N, O and S doped CF. The experiments found that $Ni(OH)_2$ nanosheets of $Ni(OH)_2/NOSCF$ decorated with ~3.3 nm sized CeO_2 NPs displayed enhanced OER performance. Compared with $Ni(OH)_2/NOSCF$, the onset potential of CeO_2 NP decorated $Ni(OH)_2/NOSCF$ decreased from 270 to 240 mV, and the Tafel slope reduced from 65 to 57 mV dec^{-1}, much better than the benchmark Ir/C. As confirmed by UV-vis and XPS results, as well as electrochemical analysis, the reasons for the enhanced OER performance result from the synergistic effect between CeO_2 NPs and $Ni(OH)_2$ nanosheets by a 1.7-fold enhancement in the generation of $Ni^{III/IV}$ active species and faster charge transfer. The high OER performance of $CeO_2/Ni(OH)_2/NOSCF$ in the present study makes CeO_2 based composites very promising electrocatalysts for water oxidation.

Acknowledgements

Notes and references

1 Y. Jiao, Y. Zheng, M. Jaroniec and S. Z. Qiao, *Chem. Soc. Rev.*, 2015, **44**, 2060–2086.

2 J. Luo, J. H. Im, M. T. Mayer, M. Schreier, M. K. Nazeeruddin, N. G. Park, S. D. Tilley, H. J. Fan and M. Graetzel, *Science*, 2014, **345**, 1593–1596.

3 B. S. Yeo and A. T. Bell, *J. Am. Chem. Soc.*, 2011, **133**, 5587–5593.

4 J. H. Wang, W. Cui, Q. Liu, Z. C. Xing, A. M. Asiri and X. P. Sun, *Adv. Mater.*, 2016, **28**, 215–230.

5 L. Duan, F. Bozoglian, S. Mandal, B. Stewart, T. Privalov, A. Llobet and L. Sun, *Nat. Chem.*, 2012, **4**, 418–423.

6 M. G. Walter, E. L. Warren, J. R. McKone, S. W. Boettcher, Q. Mi, E. A. Santori and N. S. Lewis, *Chem. Rev.*, 2011, **111**, 5815.

7 C. C. L. McCrory, S. Jung, J. C. Peters and T. F. Jaramillo, *J. Am. Chem. Soc.*, 2013, **135**, 16977–16987.

8 Z. X. Fan, Z. M. Luo, Y. Chen, J. Wang, B. Li, Y. Zong and H. Zhang, *Small*, 2016, **12**, 3908–3913.

9 D. Chen, C. Chen, Z. M. Baiyee, Z. Shao and F. Ciucci, *Chem. Rev.*, 2015, **115**, 9869–9921.

10 M. W. Louie and A. T. Bell, *J. Am. Chem. Soc.*, 2013, **135**, 12329–12337.

11 S. Pintado, S. Goberna-Ferrón, E. C. Escudero-Adán and J. R. Galán-Mascarós, *J. Am. Chem. Soc.*, 2013, **135**, 13270–13273.

12 L. Trotochaud, J. K. Ranney, K. N. Williams and S. W. Boettcher, *J. Am. Chem. Soc.*, 2012, **134**, 17253–17261.

13 Q. Yin, J. M. Tan, C. Besson, Y. V. Geletii, D. G. Musaev, A. E. Kuznetsov, Z. Luo, K. I. Hardcastle and C. L. Hill, *Science*, 2010, **328**, 342–345.

14 L. Wu, Q. Li, C. H. Wu, H. Zhu, A. Mendoza-Garcia, B. Shen, J. Guo and S. Sun, *J. Am. Chem. Soc.*, 2015, **137**, 7071–7074.

15 K. Y. Niu, F. Lin, S. Jung, L. Fang, D. Nordlund, C. C. L. McCrory, T. C. Weng, P. Ercius, M. M. Doeff and H. Zheng, *Nano Lett.*, 2015, **15**, 2498–2503.

16 R. Subbaraman, D. Tripkovic, K. C. Chang, D. Strmcnik, A. P. Paulikas, P. Hirunsit, M. Chan, J. Greeley, V. Stamenkovic and N. M. Markovic, *Nat. Mater.*, 2012, **11**, 550–557.

17 C. C. L. McCrory, S. Jung, I. M. Ferrer, S. M. Chatman, J. C. Peters and T. F. Jaramillo, *J. Am. Chem. Soc.*, 2015, **137**, 4347–4357.

18 F. Y. Cheng, T. R. Zhang, Y. Zhang, J. Du, X. P. Han and J. Chen, *Angew. Chem., Int. Ed.*, 2013, **52**, 2474–2477.

19 S. Chen and S. Z. Qiao, *ACS Nano*, 2013, **7**, 10190–10196.

20 H. Liang, F. Meng, M. Cabán-Acevedo, L. Li, A. Forticaux, L. Xiu, Z. Wang and S. Jin, *Nano Lett.*, 2015, **15**, 1421–1427.

21 J. F. Ping, Y. X. Wang, Q. P. Lu, B. Chen, J. Z. Chen, Y. Huang, Q. L. Ma, C. L. Tan, J. Yang, X. H. Cao, Z. J. Wang, J. Wu, Y. B. Ying and H. Zhang, *Adv. Mater.*, 2016, **28**, 7640–7645.

22 W. J. Zhou, X. J. Wu, X. H. Cao, X. Huang, C. L. Tan, J. Tian, H. Liu, J. Y. Wang and H. Zhang, *Energy Environ. Sci.*, 2013, **6**, 2921–2924.

23 M. Gao, W. Sheng, Z. Zhuang, Q. Fang, S. Gu, J. Jiang and Y. Yan, *J. Am. Chem. Soc.*, 2014, **136**, 7077–7084.

24 G. G. Liu, P. Li, G. X. Zhao, X. Wang, J. T. Kong, H. M. Liu, H. B. Zhang, K. Chang, X. G. Meng, T. Kako and J. H. Ye, *J. Am. Chem. Soc.*, 2016, **138**, 9128–9136.

25 Y. Zheng, M. Gao, Q. Gao, H. Li, J. Xu, Z. Wu and S. Yu, *Small*, 2015, **11**, 182–188.

26 F. Esch, S. Fabris, L. Zhou, T. Montini, C. Africh, P. Fornasiero, G. Comelli and R. Rosei, *Science*, 2005, **309**, 752–755.

27 K. Xu, P. Chen, X. Li, Y. Tong, H. Ding, X. Wu, W. Chu, Z. Peng, C. Wu and Y. Xie, *J. Am. Chem. Soc.*, 2015, **137**, 4119–4125.

28 J. X. Feng, S. H. Ye, H. Xu, Y. X. Tong and G. R. Li, *Adv. Mater.*, 2016, **28**, 4698–4703.

29 X. Yu, M. Zhang, J. Chen, Y. Li and G. Shi, *Adv. Energy Mater.*, 2015, **150**, 1501492.

30 X. Lu, W. L. Yim, B. H. R. Suryanto and C. Zhao, *J. Am. Chem. Soc.*, 2015, **137**, 2901–2907.

31 N. Cheng, Q. Liu, J. Tian, Y. Xue, A. M. Asiri, H. Jiang, Y. He and X. Sun, *Chem. Commun.*, 2015, **51**, 1616–1619.

32 J. Pu, Y. Tong, S. Wang, E. Sheng and Z. Wang, *J. Power Sources*, 2014, **250**, 250–256.

33 A. Nag, M. V. Kovalenko, J. S. Lee, W. Liu, B. Spokoyny and D. V. Talapin, *J. Am. Chem. Soc.*, 2011, **133**, 10612–10620.

34 Y. Yang, W. Que, X. Zhang, Y. Xing, X. Yin and Y. Du, *J. Hazard. Mater.*, 2016, **5**, 430–439.

35 M. A. Oliver-Tolentino, J. Vázquez-Samperio, A. Manzo-Robledo, R. D. G. González-Huerta, J. L. Flores-Moreno, D. Ramírez-Rosales and A. J. Guzmán-Vargas, *J. Phys. Chem. C*, 2014, **118**, 22432–22438.

36 Y. Shi, J. Wang, C. Wang, T. T. Zhai, W. J. Bao, J. J. Xu, X. H. Xia and H. Y. Chen, *J. Am. Chem. Soc.*, 2015, **137**, 7365–7370.

37 Y. Tian and T. Tatsuma, *J. Am. Chem. Soc.*, 2005, **127**, 7632–7637.

38 K. Priolkar, P. Bera, P. Sarode, M. Hegde, S. Emura, R. Kumashiro and N. Lalla, *Chem. Mater.*, 2002, **14**, 2120–2128.

39 H. Li, M. Yu, F. Wang, P. Liu, Y. Liang, J. Xiao, C. Wang, Y. Tong and G. Yang, *Nat. Commun.*, 2013, **4**, 1894.

40 P. Oliva, J. Leonardi and J. F. Laurent, *J. Power Sources*, 1982, **8**, 229–255.

41 C. Tang, H. S. Wang, H. F. Wang, Q. Zhang, G. L. Tian, J. Q. Nie and F. Wei, *Adv. Mater.*, 2015, **27**, 4516–4522.

42 M. S. Burke, L. J. Enman, A. S. Batchellor, S. Zou and S. W. Boettcher, *Chem. Mater.*, 2015, **27**, 7549–7558.